Dual-template synthesis of mesoporous TiO$_2$ nanotubes with structure-enhanced functional photocatalytic performance

Guangying He[a], Jinhui Zhang[a], Yun Hu[a,b,c,*], Zhaogao Bai[a], Chaohai Wei[a,c]

[a] School of Environment and Energy, South China University of Technology, Guangzhou, 510006, PR China
[b] Guangdong Provincial Key Laboratory of Atmospheric Environment and Pollution Control, Guangzhou, 510006, PR China
[c] The Key Lab of Pollution Control and Ecosystem Restoration in Industry Clusters, Guangzhou, Ministry of Education, Guangzhou, 510006, PR China

ABSTRACT

Mesoporous TiO$_2$ nanotubes (m-TiO$_2$-NTs) with outstanding photocatalytic performance have been successfully synthesized, for the first time, through a dual-template method. The dual-template method uses multi-walled carbon nanotube (CNT) as a hard template to control the morphology and cetyltrimethylammonium bromide (CTAB) as a soft template to form the mesoporous structure. The resulting m-TiO$_2$-NTs are characterized by X-ray diffraction (XRD), scanning electron microscopy (SEM), transmission electron microscopy (TEM), thermogravimetric analysis (TGA), nitrogen adsorption-desorption and X-ray photoelectron spectroscopy (XPS). Rhodamine B (RhB) and dibutyl phthalate (DBP) are used as model pollutants to evaluate the photocatalytic properties of the new materials. The m-TiO$_2$-NTs possess a multiple channel tubular structure and have higher specific surface area than TiO$_2$ nanoparticles (TiO$_2$-NPs). These features result in significantly superior photocatalytic activity for photodegradation. Specifically, the reaction rate constant for the photodegradation of RhB is 9.8 times greater with m-TiO$_2$-NTs than it is with TiO$_2$-NPs. In the case of DBP, the rate constant is 7.7 times higher. Photocatalytic removal ratios of gaseous acetaldehyde (CH$_3$CHO) and the generation of CO$_x$ (CO + CO$_2$) were detected to evaluate the decomposition ability of the materials, m-TiO$_2$-NTs showed the best CH$_3$CHO removal efficiency and the highest CO$_2$ selectivity. The active species of photocatalytic process are found to be ·OH. In addition, the m-TiO$_2$-NTs exhibit excellent thermal and photocatalytic stability even after six recycles. This work demonstrates a novel way to fabricate mesoporous TiO$_2$ nanotubes that have multiple channel tubular structure and to apply them in environmental photocatalysis.

1. Introduction

Economic development inevitably brings environmental pollution problems, especially water pollution problems. Dyes and endocrine-disrupting chemicals (EDCs), two typical pollutants that are commonly found in water, are associated with environmental problems. For example, the bright color of rhodamine B (RhB), a basic dye, can greatly reduce the penetration of light into water thereby hampering photosynthesis [1]. Also, dibutyl phthalate (DBP), a well-known EDC, has been implicated in male and female reproductive disorders, as well as metabolic and endocrine issues that can harm human health [2]. Therefore, it is important to develop an effective method to remove pollutants like RhB and DBP from the environment. Since the discovery of the photocatalytic water splitting phenomenon at a titanium dioxide (TiO$_2$) electrode in 1972 [3], many applications of semiconductor photocatalysis technology using TiO$_2$ have been developed in numerous

fields, including solar energy conversion, sensors, medication and decontamination [4–8]. Among these uses, the application of TiO$_2$ photocatalysis in environmental remediation has attracted a great deal of interest due to its superior photoactivity, chemical stability, relatively low cost and low toxicity [9,10]. TiO$_2$, with its large band gap of 3.2 eV, can be excited by ultraviolet (UV) light, leading to the generation of electrons and holes and subsequently to radical species that can participate in the decomposition of both inorganic or organic pollutants in the environment. However, the photocatalytic efficiency of conventional TiO$_2$ nanoparticles is limited by their small specific surface area, low surface adsorption capacity, tendency of particles to aggregate and low sunlight utilization [11,12].

The photocatalytic performance of semiconductors depends greatly on the morphology structure (e.g., nanoparticles, hollow spheres, nanowires or nanotubes) [13–16] which plays a key role in determining the material's physical and chemical properties, including light

* Corresponding author at: School of Environment and Energy, South China University of Technology, Guangzhou, 510006, PR China.
  E-mail address: huyun@scut.edu.cn (Y. Hu).

harvesting, surface reactions and charge transfer performance [17,18]. Due to its large specific surface area, abundant number of surface defects and ion exchange feature, TiO$_2$ nanotubes have found extensive applications in the fields of photocatalysis, electrochemical capacitors and solar cells [19,20]. There are a number of methods commonly used to fabricate TiO$_2$ nanotubes, including titanium foil anodic oxidation, alkaline hydrothermal synthesis, electrospinning and templating [21–24]. However, the nanotube arrays obtained by anodic oxidation are honeycomb-like and connected, thereby hindering the diffusion of guest molecules and the reflection of light between the tubes. Alkaline hydrothermal synthesis generates nanotubular TiO$_2$ from TiO$_2$ nanoparticles that easily aggregate thereby reducing many favorable properties, such as high specific surface area. The nanotubes prepared by electrospinning have large diameters (on the order of micrometers) and thick tube walls, which reduce the material's photocatalytic potential. In addition, the morphology of the nanotubes prepared by above methods are difficult to control. Hence, it is important have a method that can generate nanotubular TiO$_2$ in a controllable and reproducible manner.

Furthermore, the nanotube structure has some additional, unavoidable disadvantages. A small dimension of the nanotube limits mass transfer, and light has limited access to the interior of the nanotube due to its long channel and opaque walls [25,26]. Therefore, it is important to construct an accessible structure that would facilitate the diffusion of guest molecules and allow maximum penetration of lights. Mesoporous materials have broad application prospects in catalysis, adsorption, and other fields [27,28], owing to their large specific surface area and unique uniform pores. Introducing mesoporous structures on the nanotube wall will make a one-dimensional structure become to a three-dimensional structure that can greatly improve the mass transfer of guest molecules, increase the access of light to refract and reflect in the interior of the tube, and expose additional number of active sites. Interestingly, Li et al. [29] synthesized spiny titanium tubes with mesopores by solvothermal alcoholysis of TiOSO$_4$·xH$_2$SO$_4$·xH$_2$O at 110 °C. The structure was constructed by self-assembled nanosheets, resulting in a tube with a diameter of more than 2 μm and a thickness of tube wall that was about 500 nm. The spiny tubes showed the higher photodegradation of RhB activity; i.e., 1.3 times higher than that of the TiO$_2$ reference material. However, the large scale and special morphology can enhance the photocatalytic activity to a limited extent. Thus, it is important to design materials that strengthen the photocatalytic activity via the specific structure-activity relationships. To the best of our knowledge, a morphology controllable synthesis that design a specific structure to enhance the photocatalytic performance of mesoporous TiO$_2$ nanotube has not been reported.

In this work, we report on the synthesis of a mesoporous TiO$_2$ nanotube (m-TiO$_2$-NT) with a multiscale porous structure by a morphology controllable dual-template method. The preparation process of m-TiO$_2$-NT is illustrated in Scheme 1. Carbon nanotube (CNT) was used as a hard template due to its favorable nanotubular structure, and cetyltrimethylammonium bromide (CTAB) was used as a soft template and a pore-forming agent. Introducing a SiO$_2$ interlayer favors formation of nanotubes, preventing aggregation of the particles and protecting the fragile tubular structure. To evaluate the photocatalytic performance of m-TiO$_2$-NTs, photodegradation of RhB, DBP and gaseous acetaldehyde was carried on different TiO$_2$ photocatalysts. The m-TiO$_2$-NTs exhibited superior photocatalytic activity for the degradation of both RhB and DBP under UV light irradiation when compared to other TiO$_2$ photocatalysts.

2. Experimental

2.1. Materials

Multi-walled carbon nanotubes (CNTs) were purchased from Shenzhen Nanotech Port Co. Ltd. Commercial P25 was purchased from Degussa. Sodium hydroxide, hydrochloric acid, ammonia (28.0%), ethanol, cetyltrimethylammonium bromide (CTAB, AR), ethylenediamine (EN), isopropyl alcohol (IPA, AR), ethylenediaminetetraacetic acid (EDTA, AR) and potassium bromate (KBrO$_3$, AR) were purchased from Tianjin Chemical Reagent Factory. Tetraethyl orthosilicate (TEOS, AR), titanium butoxide (TBOT, AR), ethanol and Rhodamine B (RhB, AR) were purchased from Sinopharm Chemical Reagent Co. Ltd, Shanghai. Dibutyl phthalate (DBP, AR) and acetaldehyde (CH$_3$CHO, AR) were purchased from Aladdin, Shanghai. All chemicals were used as received.
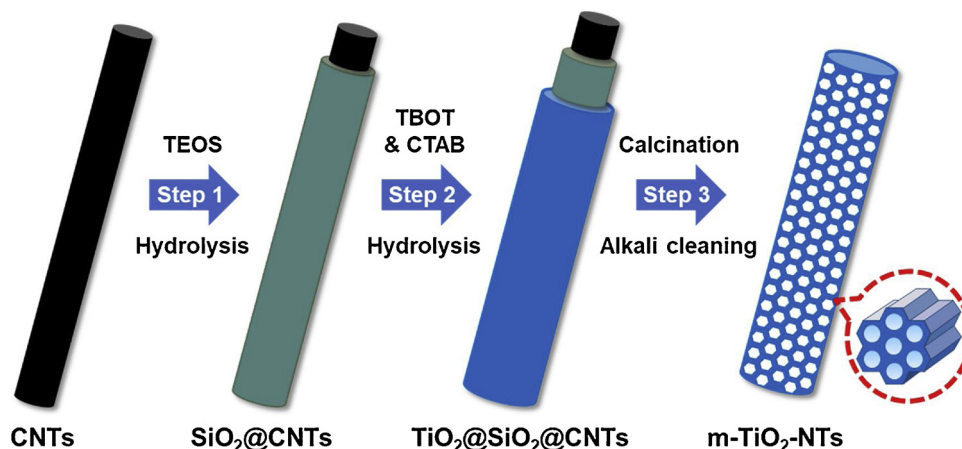
2.2. Preparation of materials
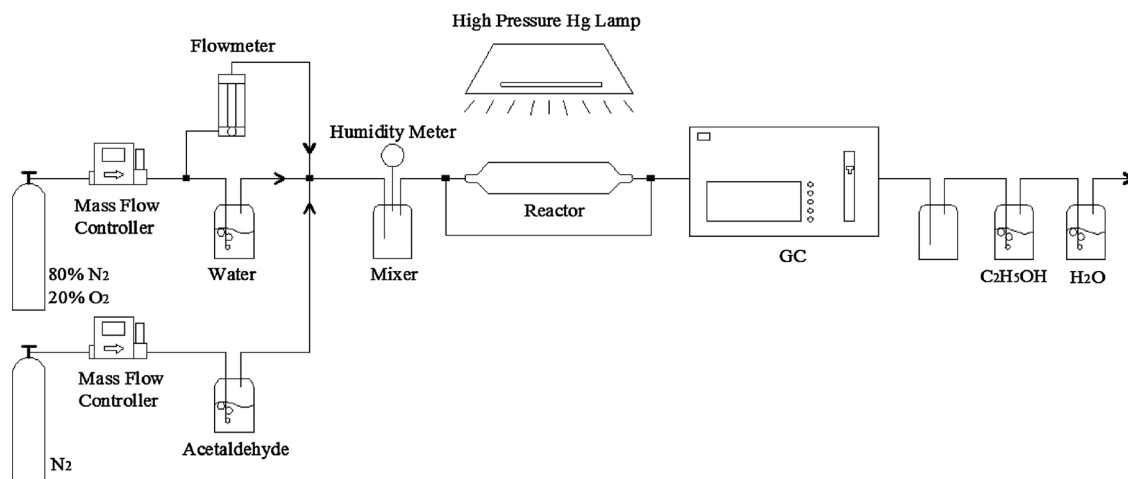
2.2.1. Preparation of SiO$_2$@CNTs

In a typical experiment, 1.1 g of CNTs was immersed in 100 mL of absolute ethanol containing 15 mL of deionized water and 4 mL of ammonia while stirring at room temperature for 30 min and 3.0 mL of TEOS was added dropwise. The reaction proceeded at room temperature for 1 h under gentle agitation. The products were centrifuged with 5 M HCl at a rate of 3500 rpm/min. Then SiO$_2$@CNTs was collected, washed with deionized water and ethanol several times, and then dried at 80 °C for 10 h.
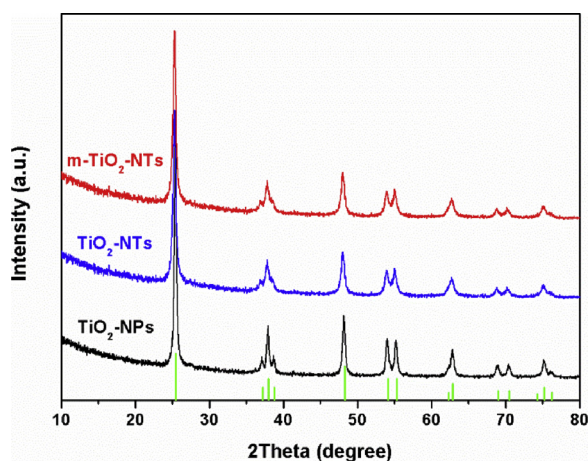
2.2.2. Preparation of TiO$_2$@SiO$_2$@CNTs

A 0.3 g amount of SiO$_2$@CNTs was impregnated in 30 mL of absolute ethanol under ultrasonic dispersing at room temperature for 30 min, and the mixture was labeled as A. At the same time, 0.788 g of CTAB was dissolved in 20 mL of absolute ethanol containing 20 mL of

Scheme 1. Schematic illustration of the synthesis of mesoporous TiO$_2$ nanotubes prepared by the dual-template method.

Scheme 2. Schematic diagram of the acetaldehyde removal system.

Fig. 1. XRD patterns of different TiO_2 photocatalysts.

Table 1
Crystallite size, BET surface area, pore volume and pore diameter of different TiO_2 photocatalysts.

Sample	Crystallite size (nm)	S_{BET} (m^2/g)	V_P (cm^3/g)	D_P (nm)
TiO_2-NPs	24.6	54.0	0.19	14.1
TiO_2-NTs	18.1	78.4	0.27	15.1
m-TiO_2-NTs	16.7	220	0.36	6.57

deionized water and 20 mL of ethanol was added dropwise to the solution which mixed a defined amount of TBOT with 30 mL ethanol under stirring at 40 °C for 24 h. The molar ratio of TBOT to deionized water is 4:1. The precipitate was collected by filtration and washed with deionized water several times before being dried at 80 °C for 10 h. Finally, the sample was calcined at 500 °C for 3 h using a heating rate of 1 °C/min. This material was denoted as TiO_2-NPs.

2.3. Characterizations

The crystal phase structures of the samples were examined by X-ray diffraction (XRD) (Bruker, D8) with Cu Kα radiation (λ = 0.15418 nm). The scan range of 2θ was 10~80°. Field emission scanning electron microscopy (FE-SEM, Hitachi, S-4800) and transmission electron microscopy (TEM, JEOL, JEM-2010) were used to examine the morphology of samples. The powder was dispersed in ethanol with ultrasonication for 30 min before the electron microscopy examination. Nitrogen adsorption-desorption isotherms were measured at 77 K with a Micromeritics Asap 2020 specific surface area analyzer. All samples were degassed at 200 °C for 3 h before measurements. Thermogravimetric analysis (TGA) was performed with a Netzsch STA449C Analyzer using a heating rate of 10 °C/min in an ambient air environment with a flow rate of 40 mL/min. X-ray photoelectron spectroscopy (XPS) was performed on a Thermo Escalab 250Xi spectrometer (Thermo, USA) with a monochromatic Al Kα source. The XPS peaks were calibrated with the C 1 s peaks at 284.8 eV of contaminant carbon. Photocurrent measurements were conducted by a CHI 660B electrochemical analyzer (Chenhua, China) at room temperature. All the experiments were carried out in a standard three-electrode system with a working electrode (photoelectrode), a platinum counter electrode and an Ag/AgCl reference electrode. The area of the electrodes is about 1×1 cm^2. 0.5 M Na_2SO_4 aqueous solution was used as the electrolyte. A 125 W high pressure mercury lamp (Philips) was used as UV light source.
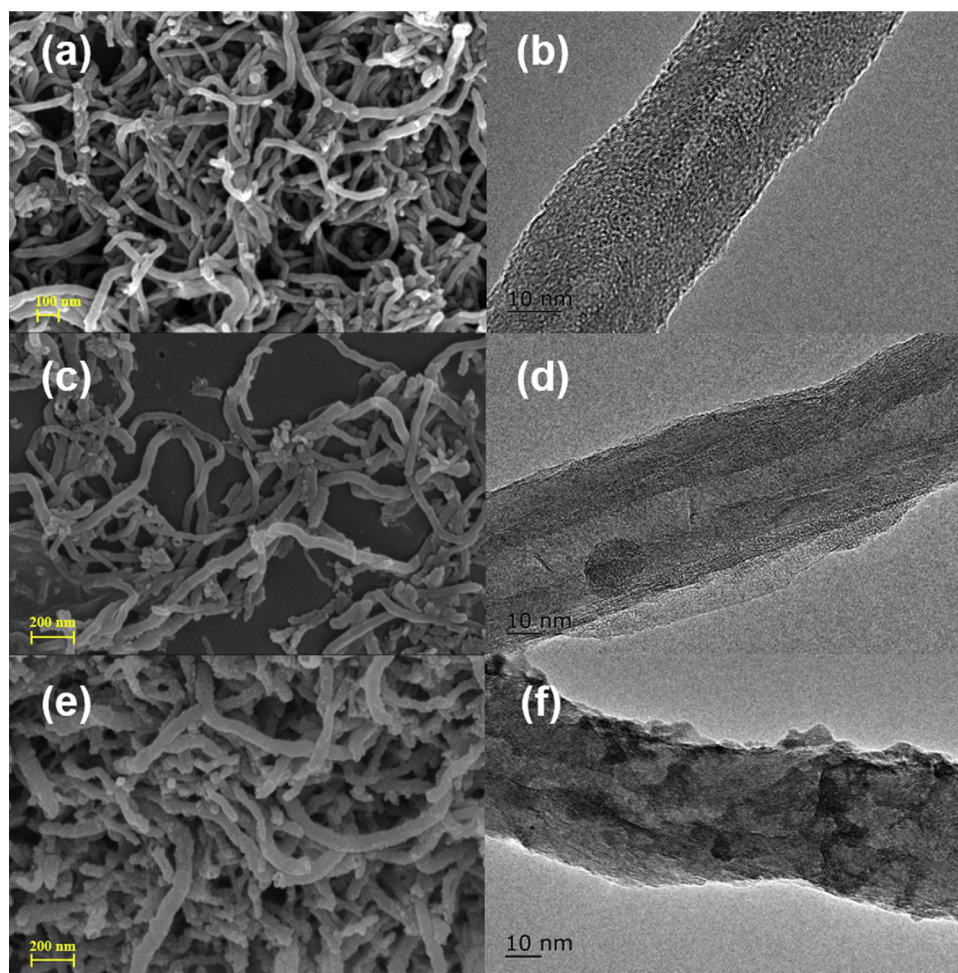
TBOT under stirring at room temperature for 30 min and it was labeled as B. Then the B was slowly added dropwise into solution A while stirring vigorously at room temperature over a 2 h period. A mixed solution containing 0.432 mL of deionized water and 1.5 mL of ethanol was dropped slowly into the above solution while stirring, and the mixture was further stirred gently for 24 h. The resulting precipitate was collected and washed with ethanol and deionized water several times before being dried at 80 °C for 10 h.

2.2.3. Preparation of m-TiO_2-NTs

0.4 g of $TiO_2@SiO_2@CNTs$ was immersed in 50 mL of ethylene diamine solution at pH = 11, and the suspension refluxed at 100 °C for 48 h. A sample was obtained by filtration, washed with deionized water and dried at 80 °C. A predetermined amount of the above sample was calcined at 600 °C for 4 h at a heating rate of 1 °C/min to remove the CNTs templates. Next, 0.2 g of the sample was added to 80 mL of 1.0 M NaOH and then autoclaved at 150 °C for 0.5 h in a 100 mL Teflon-lined autoclave. The resulting precipitate was washed with 0.1 M HCl, followed by several washes with deionized water until the filtrate was neutral. The material was then dried at 80 °C for 10 h and denoted as m-TiO_2-NTs.

2.2.4. Preparation of reference samples

The TiO_2 nanotubes without mesoporous structure were prepared via the same method as above, but without CTAB, and denoted as TiO_2-NTs. The TiO_2 nanoparticles were synthesized by the hydrolysis of TBOT. Typically, the mixed solution containing a certain amount of

Fig. 2. SEM and TEM images of (a, b) CNTs; (c, d) SiO$_2$@CNTs; (e, f) TiO$_2$@SiO$_2$@CNTs.
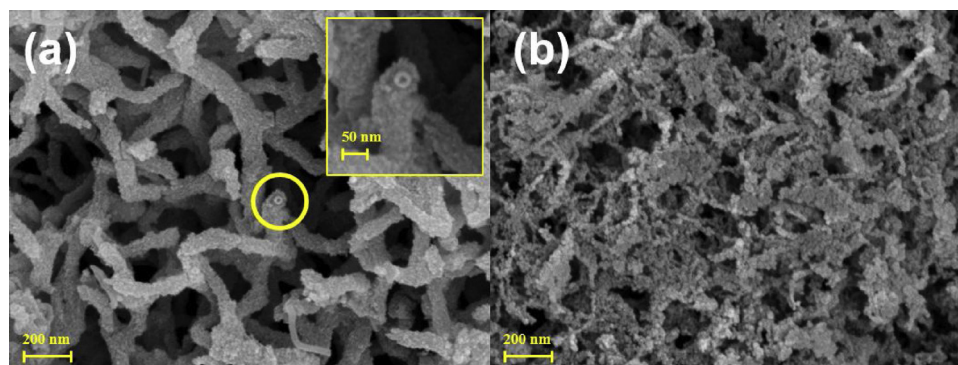

Fig. 3. SEM images of (a) TiO$_2$@CNTs; (b) m-TiO$_2$-NTs- without SiO$_2$.

2.4. Photocatalytic performance test

2.4.1. Photocatalytic degradation of RhB and DBP in water

To evaluate the photocatalytic activity of the prepared samples, a 125 W high pressure mercury lamp (Philips) was used as UV light source. The light intensity was 1.5 mW/cm^2 (UV at 365 nm), which was measured with a UVA radiometer (Photoelectric Instrument Factory of Beijing Normal University). RhB and DBP were used as representative pollutants to estimate the photocatalytic activity of the prepared samples. The photocatalytic degradations of RhB and DBP were carried out in a home-made reactor. 20 mg of a photocatalyst was added to 100 mL of solution containing either 20 mg/L RhB or 5 mg/L DBP. Before the irradiation process, the suspension was stirred in the dark for 30 min to establish adsorption-desorption equilibrium. At given time intervals during the photodegradation, 2 mL of the suspension was collected and then filtered through 0.45 μm membrane filters for analysis. The concentration of RhB was determined at the maximum absorption band (554 nm) using a UV-vis spectrophotometer (Hitachi U-3010). The concentration of DBP was determined by a high performance liquid chromatograph (HPLC, Shimadzu LC-20AT), equipped with a C18 (250 × 4.6 mm, Agilent) column. The mobile phase was a mixture of methanol and water (90:10, v/v), flowing at a rate of 1.0 mL/min. The RhB or DBP removal ratio (η) was calculated as η (%) = (1-C/C_0) × 100%, where C and C_0 are the concentrations of RhB or DBP after
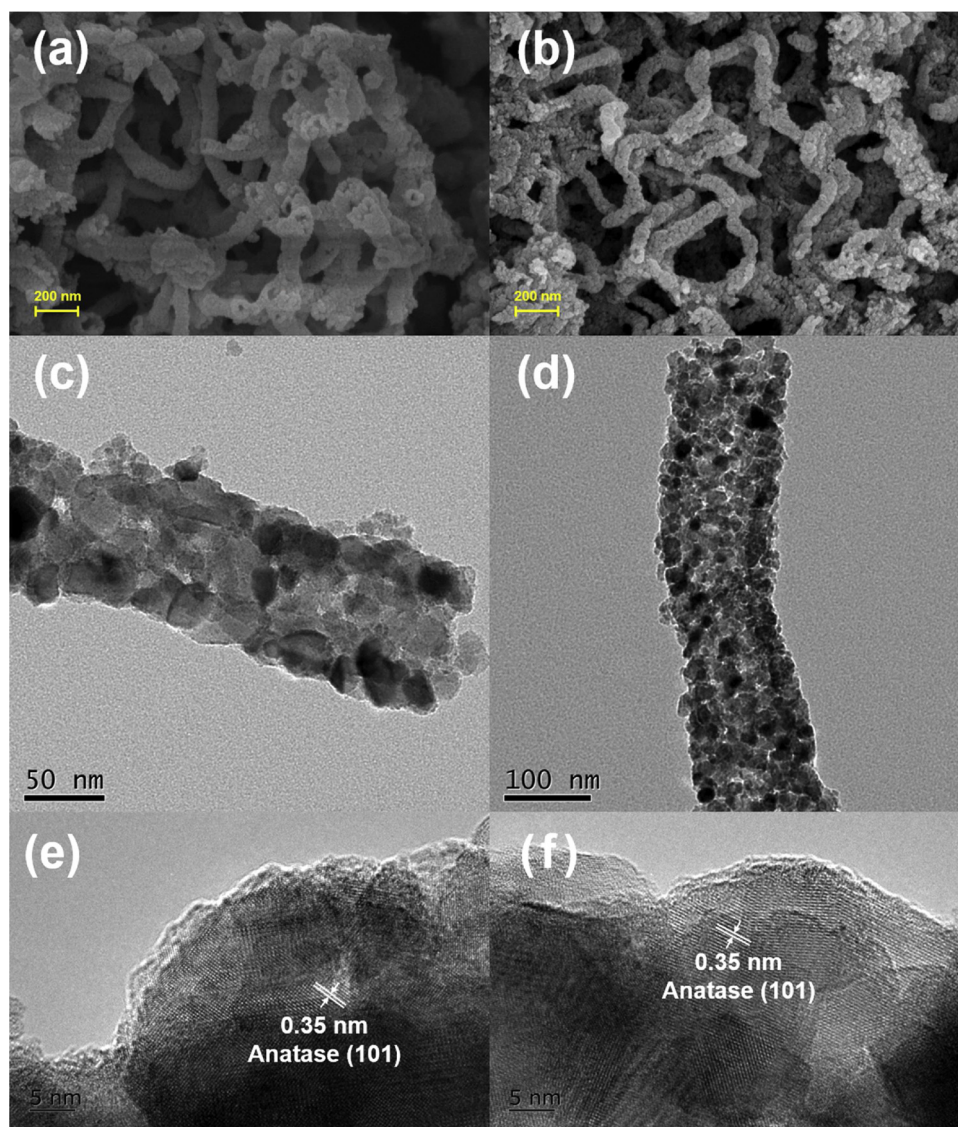
Fig. 4. SEM, TEM and HRTEM image of (a, c, e) TiO$_2$-NTs and (b, d, f) m-TiO$_2$-NTs.

and before photoreaction.

The active radical species were determined by a method similar to the photocatalytic experimental process, using IPA, EDTA and KBrO$_3$ to illustrate the presence of hydroxyl radical ($^\cdot$OH), photogenerated holes (h$^+$), and superoxide radical ($^\cdot$O$_2$$^-$), respectively.

2.4.2. Photocatalytic degradation of gaseous acetaldehyde

The photocatalytic degradation of gaseous acetaldehyde was performed at ambient temperature in a continuous acetaldehyde removal system as shown in Scheme 2. The acetaldehyde gas was obtained by flowing nitrogen into a saturator filled with acetaldehyde solution at ice bath, and the flow rate of nitrogen was 0.25 mL/min regulated by a mass flow controller. The 20 vol% O$_2$/N$_2$ compressed air was divided into two paths. One of them was served as the humidification of air, and the other one was used to transport the dry air. The humidification was obtained by bubbling air through a glass bottle containing deionized water at room temperature. The air flow was regulated by a flowmeter and the relative humidity was remained at 60%. The acetaldehyde gas was mixed with air to obtain a flow rate of 100 mL/min with 40 ppm acetaldehyde in the gas mixture. The gas was sent to a 120 mL quartz reactor with 50 mg photocatalysts. A 125 W high pressure mercury lamp (Philips) with an intensity of 50 mW/cm^2 was used as a UV light source. The concentration of the outlet acetaldehyde was determined by

a gas chromatograph (GC-2014, Shimadzu, Japan) equipped with a flame ionization detector (FID). A methanizer equipped with Ni-based catalyst was integrated into the GC system to analyze outlet CO and CO$_2$ concentration. Acetaldehyde removal ratio (η) is defined as η (%) = (C_{in}-C_{out}/C_{in})$\times$100%, where C_{in}, and C_{out} are the initial and outlet concentration (ppm) of the acetaldehyde. And the CO, CO$_2$ and CO$_X$ (CO + CO$_2$) selectivities are defined as S_{COx} (%) = C_{COx}/[2(C_{in}-C_{out})]$\times$100%, where the C_{COx} is the outlet concentration (ppm) of the CO$_x$.

3. Results and discussion

3.1. XRD analysis

The phase and crystallite structure of TiO$_2$-NPs, TiO$_2$-NTs and m-TiO$_2$-NTs photocatalysts were investigated by XRD analyses. As shown in Fig. 1, the diffraction peaks at 25.4°, 37.7° and 48° are the characteristic peaks of anatase TiO$_2$ (JCPDS 21-1272), which can be indexed to (101), (004) and (200) diffraction planes, respectively [30]. TiO$_2$-NPs, TiO$_2$-NTs and m-TiO$_2$-NTs have same obvious diffraction peaks of anatase, indicating that the calcination and alkali cleaning do not destroy the phase structure. The sharp shapes and high intensity of diffraction peaks indicated that all the TiO$_2$ samples have high
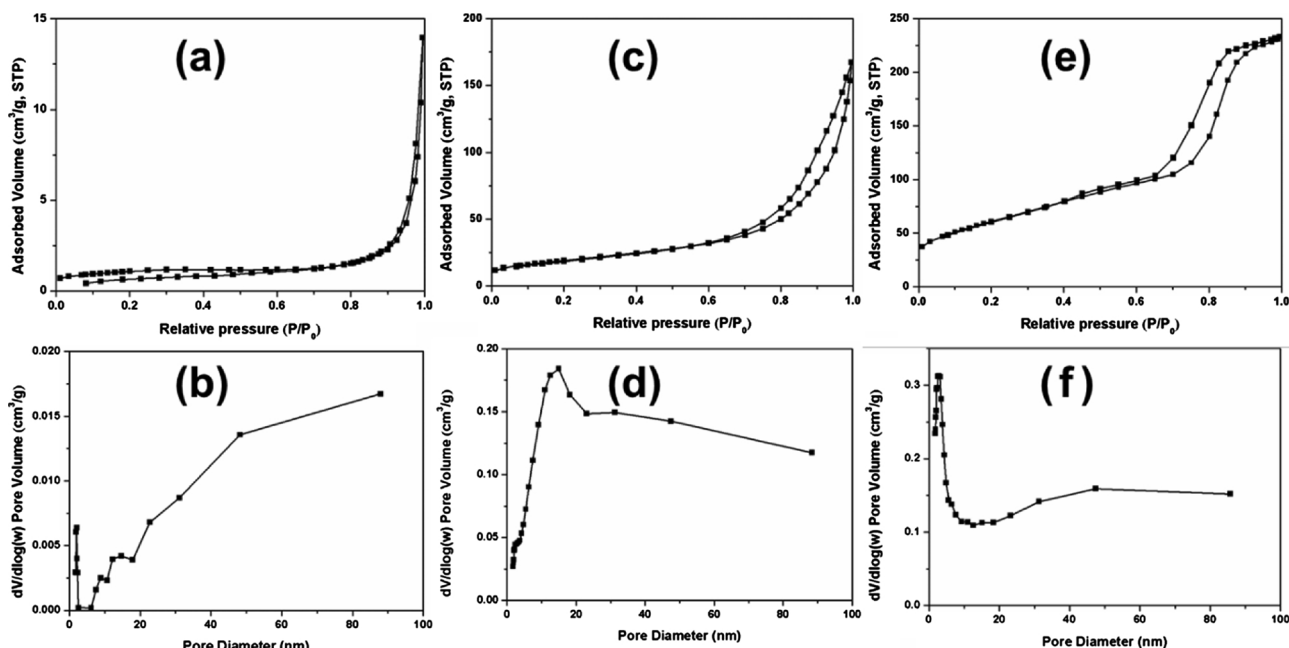
Fig. 5. N_2 adsorption-desorption isotherms and pore size distributions of (a,b) TiO_2-NPs; (c,d) TiO_2-NTs; (e,f) m-TiO_2-NTs.
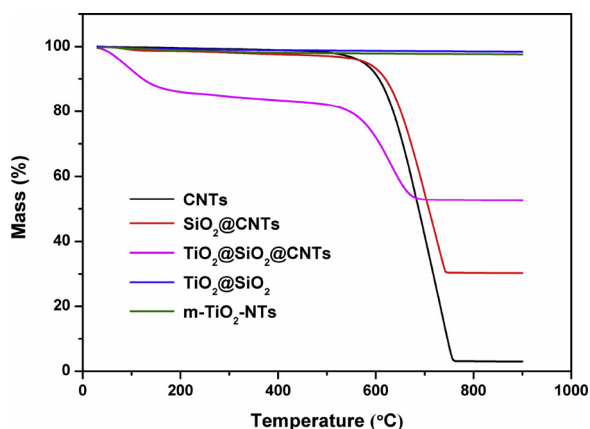

Fig. 6. TGA curves of raw CNTs, m-TiO_2-NTs and intermediate samples.

crystallinity [31]. The crystallite sizes of different TiO_2 samples were calculated by Scherrer equation, as shown in Table 1. The change of structure from nanoparticle to nanotube reduced the average crystallite size of TiO_2 from 24.6 nm (TiO_2-NPs) to 18.1 nm (TiO_2-NTs). Moreover, m-TiO_2-NTs have a smaller average crystallite size (16.7 nm) than the nanotubes, suggesting a higher surface area of the material, which is beneficial to the interfacial reaction [32].

3.2. Morphology

The morphology of the samples at different intermediate steps of the synthesis was investigated by SEM and TEM. Fig. 2a,b shows CNTs with diameters of 20˜40 nm and lengths of less than 2 μm being used as scaffolding templates. SiO_2@CNTs was prepared using tetraethyl orthosilicate (TEOS) as a silica source and ammonia as the catalyst. The SiO_2 deposition on the surface of CNTs was produced by preloading CNTs with TEOS and conducting a hydrolysis-condensation reaction in ethanol, leading to the formation of SiO_2@CNTs which contained a 20 nm thick SiO_2 interlayer (Fig. 2c,d). The surfaces of SiO_2@CNTs were smooth, confirming that the hydrolysis of TEOS was slow and the surface coating of SiO_2 on CNTs was uniform [33]. Fig. 2e,f shows the images from TiO_2@SiO_2@CNTs that were formed by further deposition

of TiO_2 on SiO_2@CNTs via the hydrolysis-condensation of titanium butoxide (TBOT). Fig. 2f shows the CNT inner core, the SiO_2 middle layer and the TiO_2 outer layer with intimate interfacial connections between them. The surface of TiO_2@SiO_2@CNTs is smooth, confirming the uniform hydrolysis of TBOT.

To investigate the effect of the SiO_2 interlayer on TiO_2 nanotubular structure, the intermediate TiO_2@CNTs was prepared by depositing TiO_2 on CNTs directly without a SiO_2 interlayer. After calcination, this material was referred to as m-TiO_2-NTs-without SiO_2. From Fig. 3a, the double layers of the walls of CNT (inner layer) and TiO_2 nanotube (outer layer) can be seen. The inset in Fig. 3a shows a cross section of a rougher TiO_2 layer coated CNT. After calcination to remove the CNTs, the nanotubular structure collapsed and was partly sintered due to the absence of the protective layer of SiO_2 during the heating process (Fig. 3b). Moreover, SiO_2-NTs were obtained by calcinating SiO_2@CNTs, demonstrating that the SiO_2 interlayer is thermostable enough to protect the mesoporous tubular structure against collapse (Fig. S1). These results illustrate that the addition of the SiO_2 interlayer was beneficial to Step 2 and 3 in Scheme1 and that it avoids the aggregation of TiO_2 and collapse of the mesoporous tubular structure.

Fig. 4 shows the typical SEM, TEM and HRTEM images of TiO_2-NTs and m-TiO_2-NTs obtained by the absence and presence of CTAB, respectively. The diameters of the two materials are in range of 100˜120 nm, and the lengths are less than 500 nm. The surfaces of TiO_2-NTs (Fig. 4a,c) and m-TiO_2-NTs (Fig. 4b,d) are rougher than that of TiO_2@SiO_2@CNTs intermediates (Fig. 2e,f), due to the crystal phase transition of TiO_2 from amorphous to anatase that results from thermal polymerization during calcination. The tube walls of TiO_2-NTs are compact, while those of m-TiO_2-NTs are loose and porous. Moreover, the surface of m-TiO_2-NTs is much rougher than that of TiO_2-NTs, owing to the presence of porosity produced by the removal of soft template CTAB during the calcination process. The unique porous tubular structure permits greater mass transfer and entry of light into the tube. The HRTEM images further confirmed the presence of anatase TiO_2-NTs and m-TiO_2-NTs. As can be seen in Fig. 4e,f, the average spacings of the lattice fringes are 0.35 nm, corresponding to the {101} planes of TiO_2 anatase. The HRTEM observation is in good agreement with the XRD result that the m-TiO_2-NTs photocatalyst has the high crystallinity. As shown in the mapping images (Fig. S2), the uniform distribution of Ti and O elements also demonstrated the successful
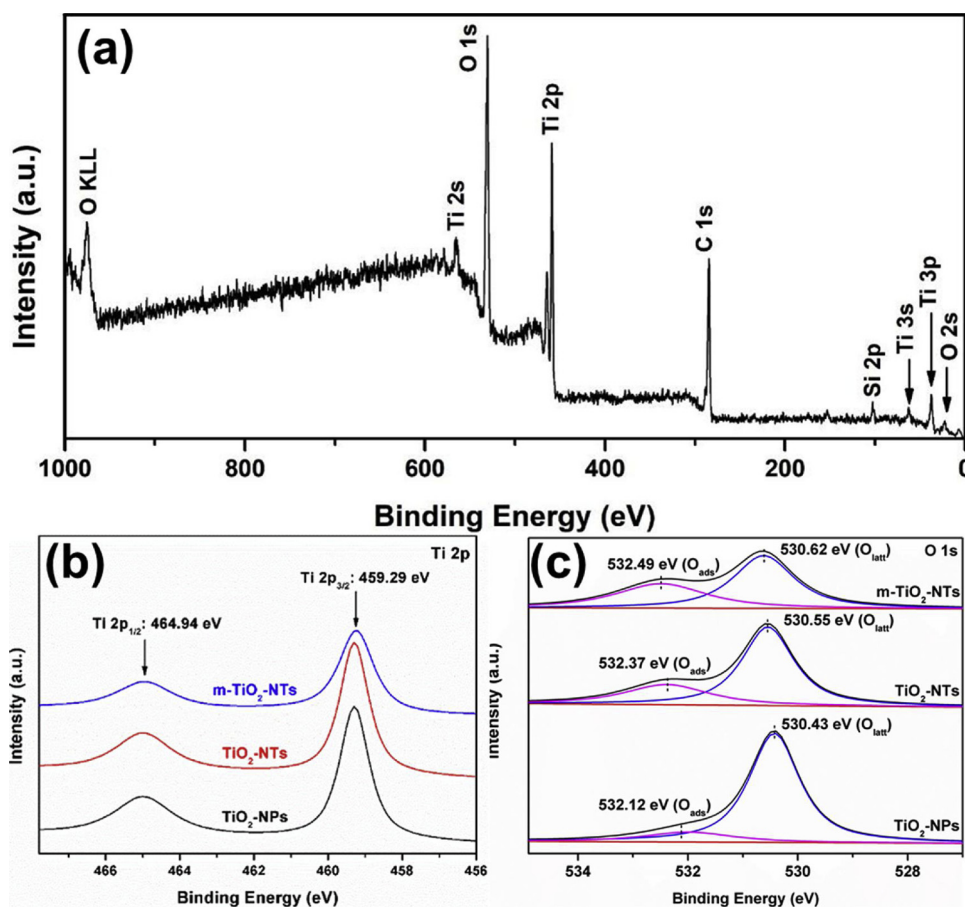
Fig. 7. (a) XPS survey spectrum of $TiO_2@SiO_2@CNTs$; high resolution XPS spectra of (b) Ti 2p and (c) O 1 s.
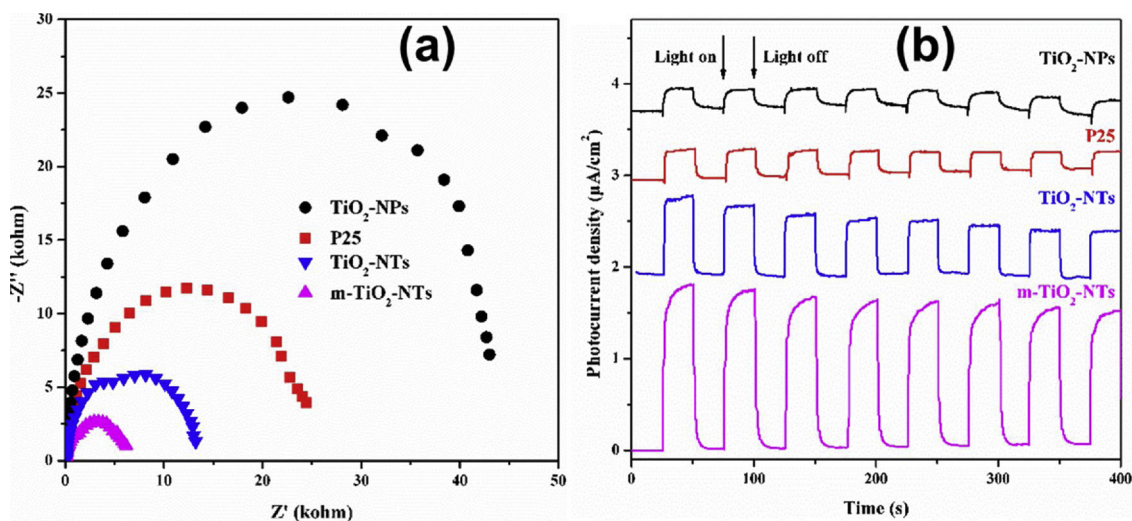

Fig. 8. The EIS Nynquist plots (a) and transient photocurrent response curves under UV light irradiation (b) of different TiO_2 photocatalysts.

formation of nanotubes.

3.3. BET analysis

To further explore the detailed structure of the photocatalysts, N_2 adsorption-desorption isotherms and the corresponding BJH pore size distributions were measured (Fig. 5). The curve of TiO_2-NPs (Fig. 5a) can be classified as a type II isotherm without the hysteresis loop, suggesting its nonporous structure. The curves of TiO_2-NTs and m-TiO_2-NTs (Fig. 5b,c, respectively) can be classified as type IV isotherms with

H3 and H1 type hysteresis loops, indicating loose slit-like pores and an ordered mesoporous network. The pore size distribution of m-TiO_2-NTs in the peak at 4 nm also corresponds to the mesoporous structure, while the wide range of 40~80 nm corresponds to the tube openings. The BET specific surface areas, average pore volumes and pore diameters of different TiO_2 photocatalysts are summarized in Table 1. Compared with TiO_2-NPs, the BET surface area, pore volume and pore size of TiO_2-NTs increased, which is ascribed to the hollow nanotube structure. The addition of CTAB in the TBOT hydrolysis process contributed to the formation of the mesoporous wall and remarkably increased the BET
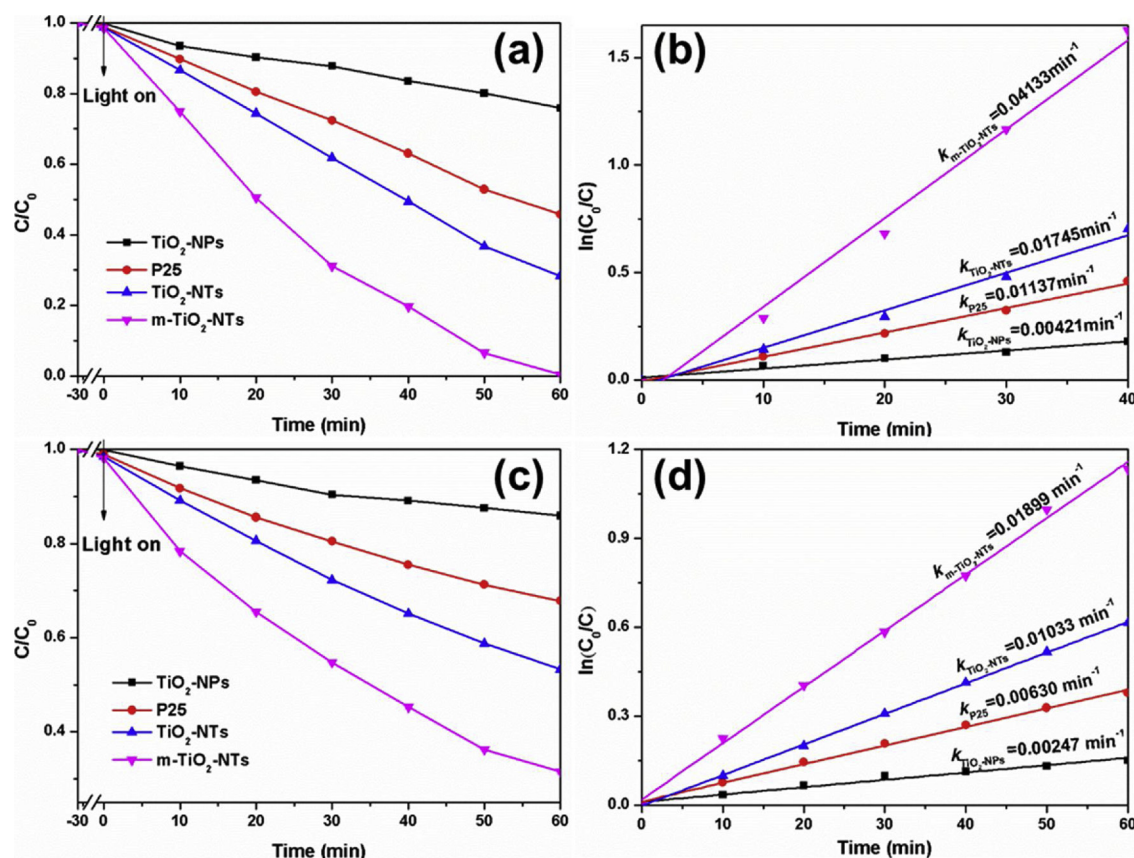
Fig. 9. Photocatalytic degradation of (a) RhB and (c) DBP over different TiO$_2$ photocatalysts under UV light irradiation; linear fit log plots of (b) RhB and (d) DBP degradation curves.

surface area of m-TiO$_2$-NTs. The BET surface area of m-TiO$_2$-NTs increased by 4.1 times and the total pore volume increased by 1.9 times when compared with TiO$_2$-NPs. There are two main scale of pore sizes of m-TiO$_2$-NTs due to the existence of mesoporous wall and tube opening (Fig. 5f), resulting in the reduction of average pore size. The mesoporous wall structure of nanotube favors the formation of a multiscale channel structure, mesopore-scale channels and macropore-scale channels, which can facilitate the mass transfer. Furthermore, the multiscale channel structure can improve the multiple reflections of light, which effectively promotes light harvesting on the inner surface of the materials. And it can greatly increase the surface area of the materials, which is contributed to the exposure of more active sites. Therefore, the mesoporous nanotube structure is expected to be associated with enhanced photocatalytic properties.

3.4. TGA analysis

To confirm the calcination temperature and the thermal stability of the samples, TGA curves of raw CNTs, m-TiO$_2$-NTs and intermediate samples are presented in Fig. 6. A significant loss of mass of raw CNTs appears in the range of 600~750 °C. This loss is also seen in TiO$_2$@SiO$_2$@CNTs, suggesting that the CNTs in TiO$_2$@SiO$_2$@CNTs intermediates can be removed in 600 °C. Therefore, 600 °C should be chosen as calcination temperature. In contrast, TiO$_2$@SiO$_2$ and m-TiO$_2$-NTs exhibited no perceivable mass loss, which is an indication of their high thermal stability. High-temperature calcination improves the crystallinity of the materials, which is beneficial to the photocatalytic activity [34].

3.5. XPS analysis

The XPS analysis was performed to investigate the chemical composition of all photocatalysts. Both survey and high-resolution spectra of Ti 2p and O 1 s are shown in Fig. 7. The binding energy for C 1 s peak at 284.8 eV was used as a reference. As shown in Fig. 7a, the survey spectrum of TiO$_2$@SiO$_2$@CNTs contains the elements Si, O and Ti. These data show that SiO$_2$ and TiO$_2$ were successfully deposited on CNTs, which is consistent with the SEM and TEM images. In Fig. 7b, the peaks at 464.94 and 459.29 eV of all samples are attributed to Ti 2p$_{1/2}$ and Ti 2p$_{3/2}$, respectively, indicating the presence of Ti^{4+} [35]. In Fig. 7c, the peak at about 530 eV is ascribed to lattice oxygen (O$_{latt}$), and the peak at about 532 eV is assigned to chemisorbed oxygen (O$_{ads}$) originated from the oxygen defects [36]. These results indicate that surface chemisorbed oxygen and lattice oxygen species exist in all TiO$_2$ photocatalysts. The ratios of chemisorbed oxygen species to lattice oxygen species (O$_{ads}$:O$_{latt}$) were calculated, as shown in Table S1. The O$_{ads}$:O$_{latt}$ ratio of m-TiO$_2$-NTs is the highest, due to larger exposed surface area and more oxygen defects. Large number of oxygen defects is contributed to a large oxygen storage capacity, and most of them are the active chemisorbed oxygen [37]. Chemisorbed oxygen species can trap photogenerated charge carriers and act as active sites, thus enhancing the photocatalytic activity [38,39].

3.6. Photoelectrochemical performance

The photoelectrochemical properties of the TiO$_2$ photocatalysts were investigated as shown in Fig. 8. EIS Nynquist plots were measured to study the mobility and interface reaction ability of the charges for the TiO$_2$ samples in Fig. 8a. The arc radius of the m-TiO$_2$-NTs photocatalyst was much smaller than those for other TiO$_2$ samples, suggesting that
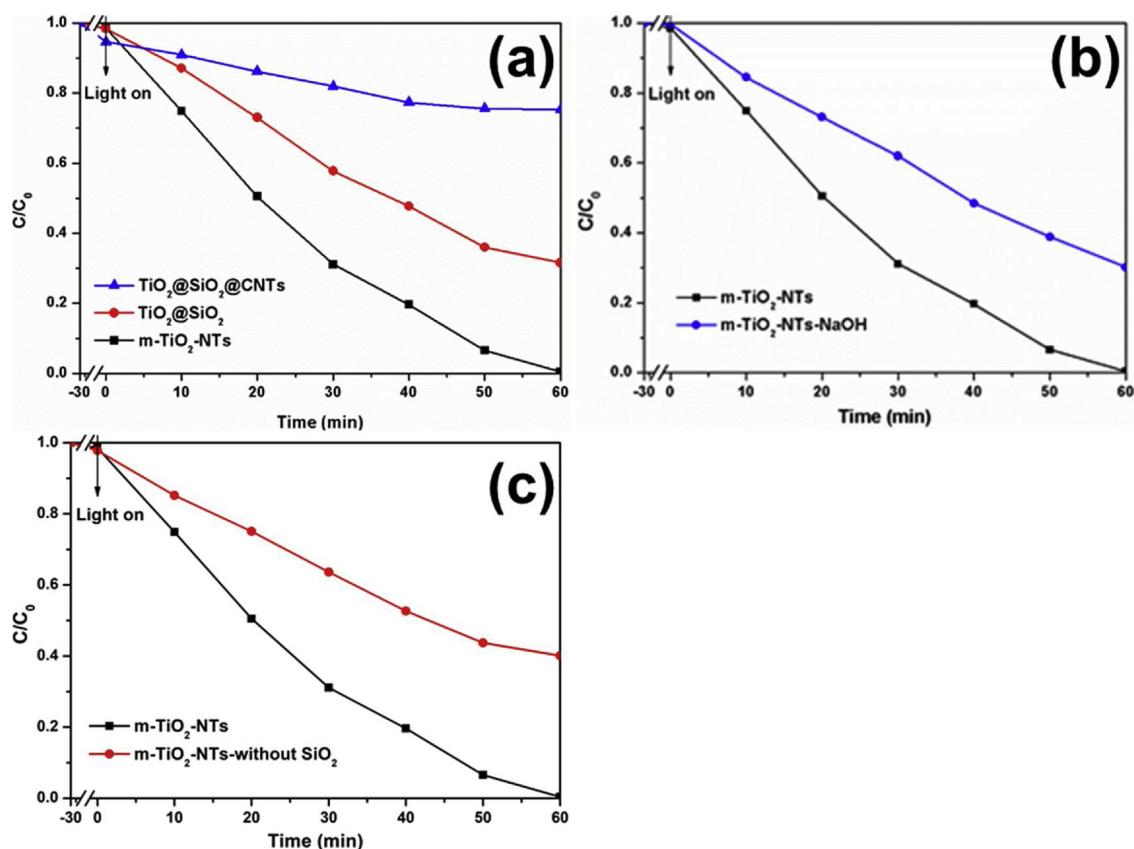
Fig. 10. Photocatalytic degradation of RhB over (a) different intermediate photocatalysts, photocatalysts (b) with different sequence of alkali cleaning and (c) with or without SiO_2 layer under UV light irradiation.
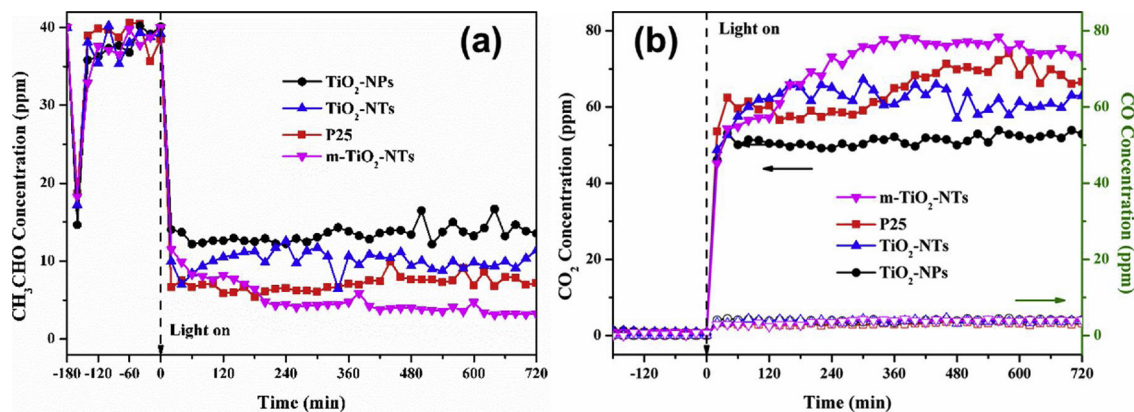

Fig. 11. Photocatalytic degradation of (a) gaseous acetaldehyde and (b) generation of CO_X over different TiO_2 photocatalysts under UV light irradiation.

the resistance of m-TiO_2-NTs was much lower than the other samples. This result confirmed that m-TiO_2-NTs possessed a high charge mobility and separation efficiency. In Fig. 8b, the transient photocurrent response curves were measured to investigate the separation efficiency of photoinduced electron-hole pairs. The photocurrent response of m-TiO_2-NTs and TiO_2-NTs were higher, more stable and more reproducible than TiO_2-NPs during on-off intermittent irradiation cycles, indicating that the nanotube structure possessed high separation efficiency of charges. This may be due to the fact that one-dimensional structure could provide a fast charge transport pathway, which could facilitate the electron transfer and restrain electron-hole pairs recombination [40,41]. Moreover, m-TiO_2-NTs had the highest photocurrent response. Since the catalyst possesses tubular channel with mesoporous walls, light can easily access to the interior of the nanotubes, leading to the formation of more photogenerated charges than

TiO_2-NTs. And electron-hole pairs were easily trapped by chemisorbed oxygen species, so the recombination of charge carriers for the m-TiO_2-NTs catalyst was inhibited. All these data showed that m-TiO_2-NTs had better photoelectrochemical properties, which was expected to be associated with enhanced photocatalytic properties [42].

3.7. Photocatalytic performance

Photocatalytic degradation of RhB and DBP under UV light irradiation was studied to determine the photocatalytic properties of different photocatalysts in Fig. 9. Fig. 9a shows that there was an insignificant amount of adsorption over all the TiO_2 samples. But in the case of photocatalysis, m-TiO_2-NTs degraded 100% of RhB in 60 min under UV light irradiation, while TiO_2-NTs, commercial TiO_2 (Degussa P25) and TiO_2-NPs degraded about 70%, 50% and 20% of RhB under the
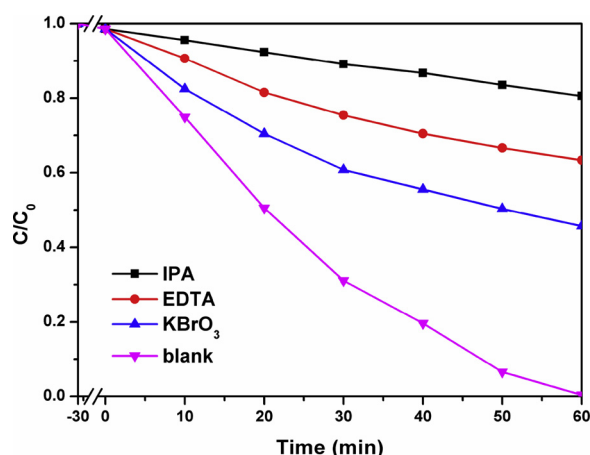
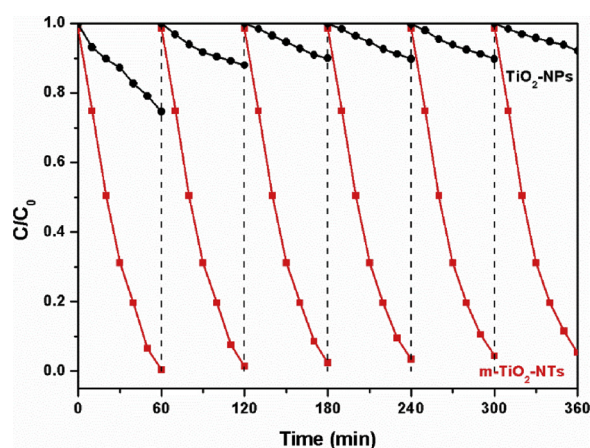**Fig. 12.** Photocatalytic degradation of RhB over m-TiO$_2$-NTs with the addition of different scavengers.

Fig. 13. Stability investigation of TiO$_2$-NPs and m-TiO$_2$-NTs.

same reaction conditions, respectively. These results illustrated that large surface area of m-TiO$_2$-NTs was beneficial to improve the photocatalysis instead of the adsorption, because the multiple channel structure with large surface area resulted in the improvement of active surface area and mass transfer. A pseudo-first order kinetic equation [$-\ln(C/C_0) = kt$] produced a good fit to the experimental data, as shown in Fig. 9b. The results demonstrated that the reaction rate constant k of m-TiO$_2$-NTs is 0.041 min^{-1}, which is about 9.8 times greater than that displayed by TiO$_2$-NPs and 2.4 greater than that observed with TiO$_2$-NTs. It is even 3.6 times greater than that of P25, which is higher than most of other TiO$_2$ nanotubes materials reported (Table S2). Moreover, the degradation of DBP by different photocatalysts under UV light irradiation was carried out. As shown in Fig. 9c, almost 70% of DBP was degraded on m-TiO$_2$-NTs within 60 min, which was more effective than on other photocatalysts. The corresponding reaction rate constant for m-TiO$_2$-NTs (0.019 min^{-1}, Fig. 9d) is about 7.7, 3.0 and 1.8 times higher than the rate constant for TiO$_2$-NPs, P25 and TiO$_2$-NTs, respectively. The greater activity of the m-TiO$_2$-NTs can be understood as a result of their multiple channel structure which can greatly enhance the mass transfer as well as the multiple reflection of light. Moreover, among all the TiO$_2$ samples, m-TiO$_2$-NTs possessed the highest O$_{ads}$:O$_{latt}$ ratio, indicating more oxygen defects in the material, which could greatly improve the photocatalytic activity.

To further evaluate of the mineralization of RhB and DBP in water, the total organic carbon (TOC) removal efficiencies were determined in Fig. S3. Apparent decreases of TOC were observed for two contaminants. After 60 min of photocatalytic reaction, 67% and 45% TOC of RhB and DBP, respectively, were eliminated, and both of them could

be effectively mineralized (100% of RhB and 99% of DBP) by the m-TiO$_2$-NTs after 4 h of UV light irradiation. These results demonstrated that there was not the decolorization of dye but the complete decomposition (into CO$_2$ and H$_2$O).

In short, the result for DBP degradation is similar to that of RhB degradation. These data explicitly illustrate that the mesoporous TiO$_2$ nanotube can effectively remove both RhB and DBP by photocatalytic degradation owing to its unique mesoporous nanotube structure.

To further demonstrate the structure-enhanced photocatalytic performance of m-TiO$_2$-NTs, the photocatalytic efficiencies of the intermediate samples were also investigated. As shown in Fig. 10a, m-TiO$_2$-NTs degraded 100% of RhB while the corresponding precursors SiO$_2$@TiO$_2$ and TiO$_2$@SiO$_2$@CNTs degraded only about 68% and 25% of RhB, respectively, in 60 min of UV light irradiation. It reveals that the material removed CNTs and SiO$_2$ have a higher photocatalytic ability due to the mesoporous structure unobstructed. Gao et al. synthesized CNTs/TiO$_2$ nanocomposites for enhancement of photocatalytic activity. However, the CNTs limited the transfer of reactant molecules, leading to only a slight enhancement of the activity; i.e., 12.8% higher than with the pure TiO$_2$ sample [43]. Removing CNTs and SiO$_2$ can make more mesopores be exposed and keep the tubes be interconnected. Therefore, it can remarkably enhance the mass transfer and multiple reflection of light, and further improve the photocatalytic activity.

The effect of the SiO$_2$ interlayer on the synthesis and photocatalytic performance of the mesoporous nanotubes was also investigated. The material, which was washed by NaOH to remove SiO$_2$ interlayer first and then calcined to remove CNTs, was denoted as m-TiO$_2$-NTs-NaOH. The degradation rate of RhB on m-TiO$_2$-NTs-NaOH was 69.8% (Fig. 10b) after 60 min of UV light irradiation, a notable decrease compared to m-TiO$_2$-NTs. This observation indicates that the SiO$_2$ interlayer played an important role in the stabilizing the nanotube structure during the heat treatment, preventing the mesoporous tubular structure from collapsing during calcination.

The photoactivity of m-TiO$_2$-NTs-without SiO$_2$ was evaluated as well. Fig. 10c shows a decrease in photocatalytic performance from 100% for m-TiO$_2$-NTs to 59.8% for m-TiO$_2$-NTs-without SiO$_2$. These data are consistent with the SEM images (Fig. 2, 3) in showing that the SiO$_2$ interlayer is essential to protecting the mesoporous nanotube structure against collapse and aggregation during the calcination. These results illustrate that the addition of the SiO$_2$ interlayer (Step 1 in Scheme1) was beneficial to the mesoporous tubular structure which can further enhance the photocatalytic performance of the materials.

In order to fully evaluate the photocatalytic performance of the TiO$_2$ samples, photocatalytic degradation of gaseous acetaldehyde (CH$_3$CHO) was carried out, and the quantitative formation of CO$_x$ (CO + CO$_2$) was checked, as shown in Fig. 11. Fig. 11a shows that all the TiO$_2$ samples possess small adsorption capacities of CH$_3$CHO, and easily reach the adsorption equilibrium in 60 min. These results were consistent with the liquid phase adsorption results as shown in Fig. 9. The m-TiO$_2$-NTs had the highest CH$_3$CHO removal ratio (about 92%) in 720 min UV light irradiation, while P25, TiO$_2$-NTs and TiO$_2$-NPs showed lower removal ratios under the same reaction conditions. Fig. 11b shows the generation of CO$_x$ over the TiO$_2$ samples, among which the m-TiO$_2$-NTs had the highest CO$_2$ selectivity (about 99%). These data illustrated that the m-TiO$_2$-NTs could decompose CH$_3$CHO into CO$_2$ and H$_2$O completely. Both liquid phase and gas phase reactions showed that m-TiO$_2$-NTs had the highest photocatalytic activity and mineralization. Based on the results of morphology and structure analyses, the promoting photocatalytic ability of m-TiO$_2$-NTs can be attributed to the multiscale channel structure, which can greatly improve the availability of light, mass transfer of guest molecules and exposure of active sites.

To gain more insight on the photocatalytic mechanism, the effect of radical scavengers on the photodegradation of RhB was investigated. IPA, EDTA and KBrO$_3$ are well-known scavengers for hydroxyl radical (·OH), photogenerated holes (h$^+$), and superoxide radical (·O$_2^-$),
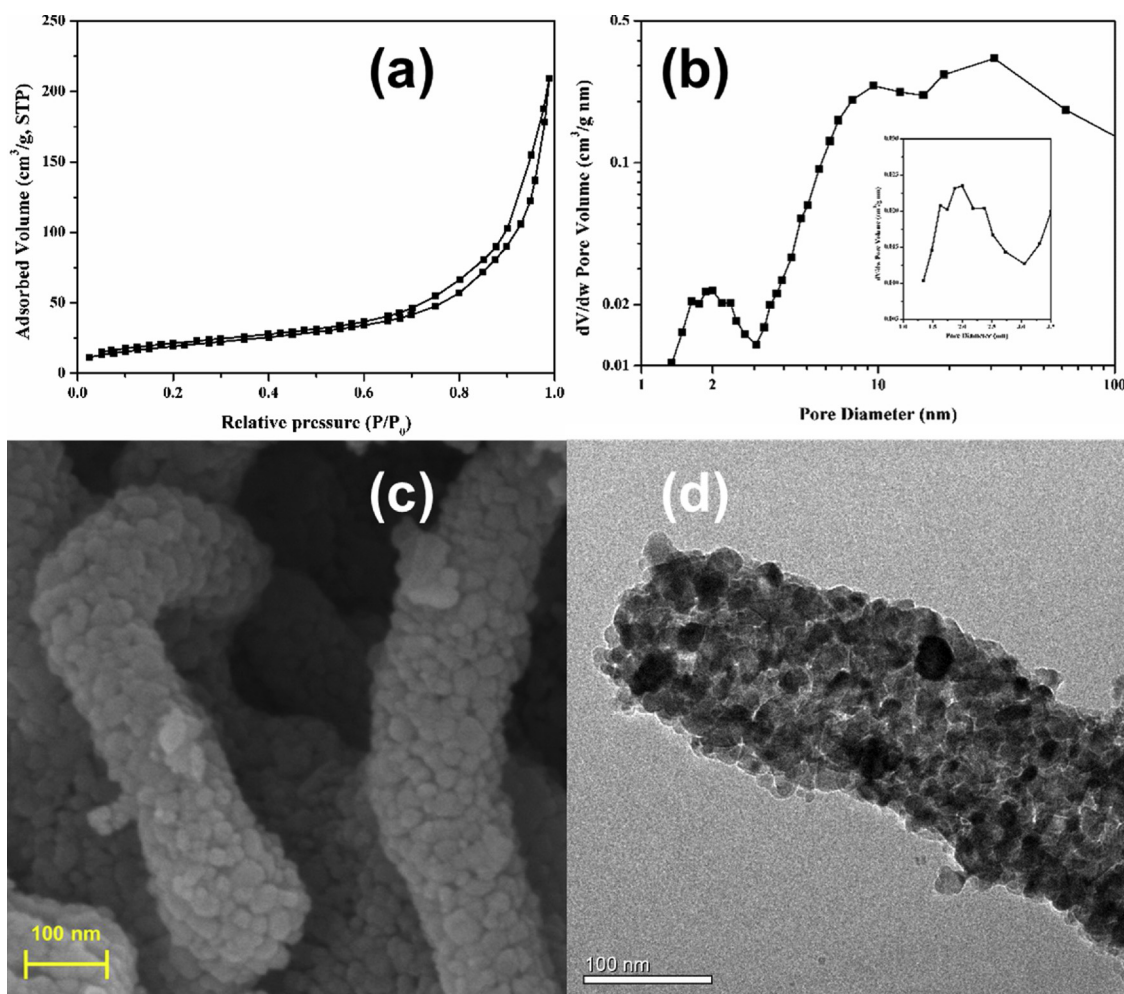
Fig. 14. Stability investigation of the used m-TiO₂-NTs: (a) N₂ adsorption-desorption isotherm, (b) pore size distribution, (c) SEM and (d) TEM images.

respectively [44]. As shown in Fig. 12, the addition of IPA caused the most significant decrease of the degradation efficiency, which suggested that ·OH was the main active species. The addition of EDTA or KBrO₃ resulted in a lower loss of activity, which implied that h⁺ and ·O₂⁻ were secondary active species for RhB photodegradation in this reaction system. In general, ·OH radicals generate dominantly on the materials' surface, and have very short diffusion distances [45]. It indicated that a considerable amount of ·OH radicals occurred on the surface of m-TiO₂-NTs, especially the inner surface, and therefore reacted with the contaminants in the tubular channels. After that the products could diffuse from the mesopores accessibly.

The stability and reusability of photocatalysts was investigated by performing recycle experiments with m-TiO₂-NTs and TiO₂-NPs photocatalysts under UV light irradiation (Fig. 13). After six recycles, the photocatalytic performance of m-TiO₂-NTs did not show any obvious decay, while that of TiO₂-NPs greatly decreased after the first round. These data show that the m-TiO₂-NTs materials were significantly more stable, durable and reusable.

In addition, the characterizations of used m-TiO₂-NTs were carried out as shown in Fig. 14. The N₂ adsorption-desorption isotherm and the corresponding BJH pore size distribution were measured. The isotherm curve of m-TiO₂-NTs (Fig. 14a) can be classified as type IV isotherm with H1 type hysteresis loop, indicating that the mesoporous structure maintained after the photocatalytic reaction. The pore size distribution (Fig. 14b) shows two peaks, which are corresponded to the mesopores in the tube walls and the macropores of the tube openings, in good agreement with that of the fresh sample (Fig. 5f). The BET specific

surface areas, average pore volumes and pore diameters of fresh and used m-TiO₂-NTs were summarized in Table S3. These data showed that no significant difference between the fresh and the used m-TiO₂-NTs. Both SEM (Fig. 14c) and TEM (Fig. 14d) images showed clear mesoporous tubular structures of the used m-TiO₂-NTs photocatalyst, and no apparent collapse was observed. These results illustrated that the m-TiO₂-NTs photocatalyst are stable, durable and reusable in both mesoporous tubular structure and photocatalytic property.

4. Conclusions

In summary, mesoporous TiO₂ nanotubes were prepared by a morphology controllable dual-template method. CNT was chosen as a hard template to control the morphology structure and CTAB was used as a soft template to form the mesoporous structure. The intervening SiO₂ layer in the TiO₂@SiO₂@CNTs precursor plays an essential role in the formation of a successful tubular structure. The m-TiO₂-NTs exhibited multiple channel tubular structure, high specific surface area, superior photocatalytic activity and excellent performance stability. The structure-enhanced functional performance resulted from the special mesoporous tubular structure, which facilitated mass transfer, increased utilization of light and exposed more active sites. Overall, the mesoporous TiO₂ nanotubes significantly improved the photocatalytic activity of traditional TiO₂ nanoparticles. This investigation also demonstrated that multiscale channel structure is a powerful strategy for manipulating the functional performance of nanomaterials which could be applied to a number of environmental pollution problems.

Acknowledgments

Appendix A. Supplementary data

Supplementary material related to this article can be found, in the online version, at doi:https://doi.org/10.1016/j.apcatb.2019.03.027.

References

[1] W.G. Kuo, Decolorizing dye wastewater with Fenton's reagent, Water Res. 26 (1992) 881–886.

[2] X. Dong, X. Qiu, S. Meng, H. Xu, X. Wu, M. Yang, Proteomic profile and toxicity pathway analysis in zebrafish embryos exposed to bisphenol a and di-n-butyl phthalate at environmentally relevant levels, Chemosphere 193 (2018) 313–320.

[3] A. Fujishima, K. Honda, Electrochemical photolysis of water at a semiconductor electrode, Nature 238 (1972) 37.

[4] Y. Wang, J. Tang, Z. Peng, Y. Wang, D. Jia, B. Kong, A.A. Elzatahry, D. Zhao, G. Zheng, Fully Solar-Powered photoelectrochemical conversion for simultaneous energy storage and chemical sensing, Nano Lett. 14 (2014) 3668–3673.

[5] W. Ouyang, F. Teng, X. Fang, High performance BiOCl Nanosheets/TiO$_2$nanotube arrays heterojunction UV photodetector: The influences of Self-Induced inner electric fields in the BiOCl nanosheets, Adv. Funct. Mater. 28 (2018) 1707178.

[6] H. Xu, S. Ouyang, L. Liu, P. Reunchan, N. Umezawa, J. Ye, Recent advances in TiO2-based photocatalysis, J. Mater. Chem. A 2 (2014) 12642.

[7] Z. Bai, Y. Hu, S. Yan, W. Shan, C. Wei, Preparation of mesoporous SiO$_2$/Bi$_2$O$_3$/TiO$_2$ superhydrophilic thin films and their surface self-cleaning properties, RSC Adv. 7 (2017) 1966–1974.

[8] J.B. Joo, I. Lee, M. Dahl, G.D. Moon, F. Zaera, Y. Yin, Controllable synthesis of mesoporous TiO$_2$hollow shells: toward an efficient photocatalyst, Adv. Funct. Mater. 23 (2013) 4246–4254.

[9] Q. Xiang, J. Yu, M. Jaroniec, Enhanced photocatalytic H$_2$-production activity of graphene-modified titania nanosheets, Nanoscale 3 (2011) 3670.

[10] X. Song, Y. Hu, M. Zheng, C. Wei, Solvent-free in situ synthesis of g-C$_3$N$_4$/{001}TiO$_2$ composite with enhanced UV- and visible-light photocatalytic activity for NO oxidation, Appl. Catal. B: Environ. 182 (2016) 587–597.

[11] R. Asahi, T. Morikawa, T. Ohwaki, K. Aoki, Y. Taga, Visible-light photocatalysis in nitrogen-doped titanium oxides, Science 293 (2001) 269–271.

[12] X. Chen, S. Shen, L. Guo, S.S. Mao, Semiconductor-based photocatalytic hydrogen generation, Chem. Rev. 110 (2010) 6503–6570.

[13] Y. Hu, X. Song, S. Jiang, C. Wei, Enhanced photocatalytic activity of Pt-doped TiO$_2$ for NO$_x$ oxidation both under UV and visible light irradiation: a synergistic effect of lattice Pt^{4+}and surface PtO, Chem. Eng. J. 274 (2015) 102–112.

[14] G. Zhang, H.B. Wu, T. Song, U. Paik, X.W. Lou, TiO$_2$ hollow spheres composed of highly crystalline nanocrystals exhibit superior lithium storage properties, Angew. Chemie Int. Ed. Engl. 53 (2014) 12590–12593.

[15] X. Zhou, N. Liu, P. Schmuki, Photocatalysis with TiO$_2$ nanotubes: "colorful" reactivity and designing Site-Specific photocatalytic centers into TiO$_2$ nanotubes, ACS Catal. 7 (2017) 3210–3235.

[16] M. Ge, C. Cao, J. Huang, S. Li, Z. Chen, K. Zhang, S.S. Al-Deyab, Y. Lai, A review of one-dimensional TiO$_2$ nanostructured materials for environmental and energy applications, J. Mater. Chem. A 4 (2016) 6772–6801.

[17] U. Banin, Y. Ben-Shahar, K. Vinokurov, Hybrid semiconductor–metal nanoparticles: from architecture to function, Chem. Mater. 26 (2013) 97–110.

[18] H.G. Yang, H.C. Zeng, Synthetic architectures of TiO$_2$/H$_2$Ti$_5$O$_{11}$·H$_2$O, ZnO/H$_2$Ti$_5$O$_{11}$·H$_2$O, ZnO/TiO$_2$/H$_2$Ti$_5$O11·H$_2$O, and ZnO/TiO$_2$ nanocomposites, J. Am. Chem. Soc. 127 (2005) 270.

[19] M. Adachi, Y. Murata, M. Harada, S. Yoshikawa, Formation of titania nanotubes with high photo-catalytic activity, Chem. Lett. 29 (2000) 942–943.

[20] D. Kuang, J. Brillet, P. Chen, M. Takata, S. Uchida, H. Miura, K. Sumioka, S.M. Zakeeruddin, M. Grätzel, Application of highly ordered TiO2 nanotube arrays in flexible Dye-Sensitized solar cells, ACS Nano 2 (2008) 1113–1116.

[21] Y. Yang, L.C. Kao, Y. Liu, K. Sun, H. Yu, J. Guo, S.Y.H. Liou, M.R. Hoffmann, Cobalt-Doped black TiO$_2$ nanotube array as a stable anode for oxygen evolution and electrochemical wastewater treatment, ACS Catal. 8 (2018) 4278–4287.

[22] Y. Lan, X.P. Gao, H.Y. Zhu, Z.F. Zheng, T.Y. Yan, F. Wu, S.P. Ringer, D.Y. Song, Titanate nanotubes and nanorods prepared from rutile powder, Adv. Funct. Mater. 15 (2005) 1310–1318.

[23] N. Qin, J. Xiong, R. Liang, Y. Liu, S. Zhang, Y. Li, Z. Li, L. Wu, Highly efficient photocatalytic H$_2$ evolution over MoS$_2$/CdS-TiO$_2$ nanofibers prepared by an electrospinning mediated photodeposition method, Appl. Catal. B: Environ. 202 (2017) 374–380.

[24] J. Fan, L. Zhao, J. Yu, G. Liu, The effect of calcination temperature on the microstructure and photocatalytic activity of TiO$_2$-based composite nanotubes prepared by an in situ template dissolution method, Nanoscale 4 (2012) 6597.

[25] I. Paramasivam, H. Jha, N. Liu, P. Schmuki, A review of photocatalysis using self-organized TiO$_2$ nanotubes and other ordered oxide nanostructures, Small 8 (2012) 3073.

[26] C.B.D. Marien, T. Cottineau, D. Robert, P. Drogui, TiO$_2$ nanotube arrays: influence of tube length on the photocatalytic degradation of Paraquat, Appl. Catal. B: Environ. 194 (2016) 1–6.

[27] V. Hiremath, A.H. Jadhav, H. Lee, S. Kwon, J.G. Seo, Highly reversible CO$_2$ capture using amino acid functionalized ionic liquids immobilized on mesoporous silica, Chem. Eng. J. 287 (2016) 602–617.

[28] M. Wu, Q. Meng, Y. Chen, L. Zhang, M. Li, X. Cai, Y. Li, P. Pyu, L. Zhang, J. Shi, Large pore-sized hollow mesoporous organosilica for redox-responsive gene delivery and synergistic cancer chemotherapy, Adv. Mater. 28 (2016) 1963–1969.

[29] G. Li, J. Liu, G. Jiang, Facile synthesis of spiny mesoporous titania tubes with enhanced photocatalytic activity, Chem. Commun. 47 (2011) 7443.

[30] M. Liu, L. Piao, W. Lu, S. Ju, L. Zhao, C. Zhou, H. Li, W. Wang, Flower-like TiO2 nanostructures with exposed {001} facets: facile synthesis and enhanced photocatalysis, Nanoscale 2 (2010) 1115.

[31] K. Maeda, Z-Scheme water splitting using two different semiconductor photocatalysts, ACS Catal. 3 (2013) 1486–1503.

[32] Q. Xiang, K. Lv, J. Yu, Pivotal role of fluorine in enhanced photocatalytic activity of anatase TiO$_2$ nanosheets with dominant (001) facets for the photocatalytic degradation of acetone in air, Appl. Catal. B: Environ. 96 (2010) 557–564.

[33] H. Huang, Y. Wang, C. Zou, J. Tao, D. Qu, X. Ma, P. Liu, Y. Wan, Y. Xu, Titania Tube-in-Tube scaffolds with Multilength-Scale structural hierarchy and Structure-Enhanced functional performance, J. Phys. Chem. C 119 (2015) 17552–17560.

[34] S. Nishioka, J. Hyodo, J.J.M. Vequizo, S. Yamashita, H. Kumagai, K. Kimoto, A. Yamakata, Y. Yamazaki, K. Maeda, Homogeneous electron doping into non-stoichiometric strontium titanate improves its photocatalytic activity for hydrogen and oxygen evolution, ACS Catal. 8 (2018) 7190–7200.

[35] Y.R. Smith, B. Sarma, S.K. Mohanty, M. Misra, Light-Assisted anodized TiO$_2$ nanotube arrays, ACS Appl. Mater. Interfaces 4 (2012) 5883–5890.

[36] J. Yan, G. Wu, N. Guan, L. Li, Z. Li, X. Cao, Understanding the effect of surface/bulk defects on the photocatalytic activity of TiO$_2$: anatase versus rutile, Phys. Chem. Chem. Phys. 15 (2013) 10978.

[37] W. Yang, C. Li, H. Wang, X. Li, W. Zhang, H. Li, Cobalt doped ceria for abundant storage of surface active oxygen and efficient elemental mercury oxidation in coal combustion flue gas, Appl. Catal. B: Environ. 239 (2018) 233–244.

[38] Y. Li, X. Chen, C. Wang, C. Zhang, H. He, Sodium enhances Ir/TiO$_2$ activity for catalytic oxidation of formaldehyde at ambient temperature, ACS Catal. 8 (2018) 11377–11385.

[39] T.G. Ulusoy, A. Ghobadi, A.K. Okyay, Surface engineered angstrom thick ZnO-sheathed TiO$_2$ nanowires as photoanodes for performance enhanced dye-sensitized solar cells, J. Mater. Chem. A 2 (2014) 16867–16876.

[40] Y. Peng, K.K. Wang, T. Liu, J. Xu, B.G. Xu, Synthesis of one-dimensional Bi$_2$O$_3$-Bi$_2$O$_{2.33}$ heterojunctions with high interface quality for enhanced visible light photocatalysis in degradation of high-concentration phenol and MO dyes, Appl. Catal. B: Environ. 203 (2017) 946–954.

[41] J. Tian, Z. Zhao, A. Kumar, R.I. Boughton, H. Liu, Recent progress in design, synthesis, and applications of one-dimensional TiO$_2$ nanostructured surface heterostructures: a review, Chem. Soc. Rev. 43 (2014) 6920–6937.

[42] Y. Jia, S. Zhan, S. Ma, Q. Zhou, Fabrication of TiO$_2$-Bi$_2$WO$_6$ binanosheet for enhanced solar photocatalytic disinfection of E. coli: insights on the mechanism, ACS Appl. Mater. Interfaces 8 (2016) 6841–6851.

[43] B. Gao, G.Z. Chen, G. Li Puma, Carbon nanotubes/titanium dioxide (CNTs/TiO$_2$) nanocomposites prepared by conventional and novel surfactant wrapping sol-gel methods exhibiting enhanced photocatalytic activity, Appl. Catal. B: Environ. 89 (2009) 503–509.

[44] H. Zhang, R. Zong, J. Zhao, Y. Zhu, Dramatic visible photocatalytic degradation performances due to synergetic effect of TiO$_2$ with PANI, Environ. Sci. Technol. 42 (2008) 3803.

[45] W. Dong, Y. Sun, W. Hua, Y. Yao, G. Zhuang, X. Lv, Q. Ma, D. Zhao, Preparation of secondary mesopores in mesoporous anatase-silica nanocomposites with Unprecedented-High photocatalytic degradation performances, Adv. Funct. Mater. 26 (2016) 964–976.